Iron oxide nanoparticles synthesized by a glycine-modified coprecipitation method: Structure and magnetic properties

A. Omelyanchik [a,b,*], A.S. Kamzin [c], A.A. Valiullin [d], V.G. Semenov [e], S.N. Vereshchagin [f], M. Volochaev [g,h], A. Dubrovskiy [g], T. Sviridova [i], I. Kozenkov [a], E. Dolan [b], D. Peddis [b,j], A. Sokolov [g,h], V. Rodionova [a]

[a] Immanuel Kant Baltic Federal University, Kaliningrad, Russia
[b] Department of Chemistry and Industrial Chemistry (DCIC), University of Genova, Genova, Italy
[c] Ioffe Institute of Russian Academy of Science (RAS), St. Petersburg, Russia
[d] Kazan Federal University, Kazan, Russia
[e] St. Petersburg State University, St. Petersburg, Russia
[f] Institute of Chemistry and Chemical Technology, Federal Research Center Siberian branch RAS, Krasnoyarsk, Russia
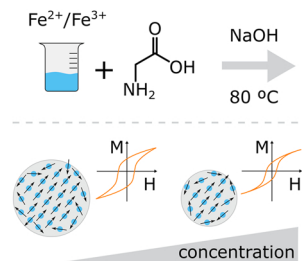[g] Kirensky Institute of Physics, Federal Research Center KSC SB RAS, Krasnoyarsk, Russia
[h] Siberian Federal University, Krasnoyarsk, Russia
[i] The National University of Science and Technology MISIS, Moscow, Russia
[j] Institute of Structure of Matter–CNR, Monterotondo Stazione, 00016 Rome, Italy

GRAPHICAL ABSTRACT

ARTICLE INFO

ABSTRACT

Iron oxide magnetic nanoparticles (MNPs) are of interest in biomedicine and research owing to their moderate cytotoxicity and advanced properties, such as extensive surface-to-volume ratio and possibilities for tailoring their functionality through surface chemistry. To date, various approaches have been used for the synthesis of MNPs with controllable structural properties and various coatings to enhance their stability and functionality. This study describes a modified one-step method of coprecipitation in the presence of glycine allowing the production of particles with controllable size and in situ surface decoration. The effect of different glycine concentrations on the morphostructural and magnetic properties of iron oxide MNPs is studied. The particle size

is reduced from 10.2 ± 0.3 to 7.2 ± 0.5 nm by increasing the glycine concentration from 0.06 up to 0.60 mol. The magnetic properties of obtained particles were tracked by SQUID magnetometry and Mössbauer spectroscopy. All samples of glycine capped iron oxide MNPs showed superparamagnetic behaviour at room temperature with maximal value of the saturation magnetization of 69 ± 4 Am^2/kg. The results show the optimal concentration range of glycine which can be used in this method: a lower concentration than 0.15 mol does not affect the properties of obtained particles while higher concentrations than 0.3 mol lead to the reduction of magnetic properties (the saturation magnetisation reduces to 59 ± 3 Am^2/kg when glycine concentration was 0.6 mol). The proposed economic and environment-friendly approach can be utilized to synthesise $-NH_2$ functionalised MNPs for biomedical or wastewater treatment.

1. Introduction

Magnetic nanoparticles (MNPs) are currently being studied intensively for a range of biomedical applications [1–5], particularly for cancer treatment via both targeted hyperthermia and drug delivery, as well as in diagnostics, for example, in magnetic resonance imaging (MRI) for use as contrast agents. An array of MNP materials exist for these applications, with ferrimagnetic iron oxides (magnetite Fe_3O_4 and maghemite γ-Fe_2O_3) being of particular note due to a favourable compromise between biocompatibility and magnetic properties (saturation magnetisation) [6–9]. The magnetic properties of iron oxide MNPs can be enhanced by doping with other metal ions, however, compared with other magnetic materials only iron is involved in so many functions of the human body and actively involved in metabolism (the human body contains about 4 g of iron [10]). Thus, among inorganic MNPs only iron oxides Fe_3O_4 and γ-Fe_2O_3 were approved by Food and Drug Administration (FDA) for use in the clinic and can be considered to be biocompatible [11,12]. The most significant advances in the use of MNPs appear to be related to the design of multifunctional platforms allowing simultaneous implementation of several diagnostic and therapeutic methods in the theranostic approach [13,14].

To use iron oxide MNPs, it is necessary to control their magnetic and morphostructural properties, which can be achieved by adjustment of the synthesis procedure. Various synthesis methods have been developed to obtain Fe_3O_4 and γ-Fe_2O_3 MNPs [15]. This can be done by coprecipitation, hydrothermal synthesis, sol-gel and other methods (see, for example, [16–18] and references therein). The Massart method of coprecipitation ([19]) is one of the most frequently used since it is robust and allows for production of a large volume of particle suspension in a one-pot synthesis. There are several strategies to improve this method to better control particle size and shape distribution, which in turn impact overall magnetic properties. One of those strategies is the addition of a capping agent to the metal ion solution prior to the precipitation reaction [20]. A capping agent is usually some organic molecule with a functional group (e.g., amino or carboxyl) that can bind with the particle surface and inhibit the further growth of the MNPs once the desired volume is reached [21,22]. Moreover, the surface decoration with some organic molecules provides additional functionality, better colloidal stability and control of magnetic properties [3,22,23].

The free $-NH_2$ groups can be further functionalised by polymers or other biomolecules for specific applications. For example, recently iron oxide MNPs were linked to specific antibodies for the SARS-CoV-2 and used for high-quality RNA extraction [24,25]. The efficiency of this approach for further detection of the SARS-CoV-2 virus by to real-time reverse transcription polymerase chain reaction (RT-PCR) assay on a large scale was confirmed by clinical tests. Thus, the development of economically relevant methods allowing for production of large quantities of functionalized MNPs is highly demanded.

Hamed Nosrati et al. proposed a novel synthesis procedure involving in situ surface coating with different amino acids [26], which is both simple and highly efficient. Amino acid coatings of this type, particularly glycine which shows high adsorption through its carboxyl end [27], present excellent opportunities for more versatile biomedical applications both giving good stability, and allowing for further

conjugation using the exposed amino group [28–30]. It was shown that the glycine-coated iron oxide MNPs showed high r_2 relaxivity and magnetic hyperthermia performance together with moderate cytotoxicity effect on primary mouse fibroblasts (L929) and human cervical cancer cells (HeLa) [31]. Thus, glycine-coated MNPs have the potential for use in both therapy and diagnostics of cancers, moreover as mentioned by the authors of ref. [31], such particles can be further conjugated with biomolecules or drugs for targeted drug delivery and other bioapplications.

The glycine-functionalised MNPs have promising environmental applications, allowing for the complexation and removal of harmful metal ions in water [32–34]. In particular, a removal efficiency for Cu (II) and Pb(II) ions from water of more than 90% can be achieved by magnetically separable and reusable MNPs [32,33]. Hence, glycine-coated MNPs with controlled structural and magnetic properties are of fundamental interest for biomedicine, environmental and other applications. Nevertheless, in the previous work [26], the MNPs prepared with glycine showed the lowest value of saturation magnetisation compared with other tested amino acids.

From the point of view of magnetic properties, the magnetically disordered surfaces arising due to the broken symmetry at the interface of the magnetic with the nonmagnetic (para- or diamagnetic) phase and spin disorder around defects play an important role in small magnetic particles [35]. The frequently observed phenomenon related to the deviation of surface spins is the so-called "magnetic dead layer" which usually leads to a decrease in saturation magnetization and an increase in anisotropy [36]. To keep high magnetic properties, it is important to precisely control the particle growth process by the optimisation of synthesis conditions. This can be achieved, for example, by adding the ligands containing amine groups with chelating properties preventing particle growth and temperature during the coprecipitation process [37].

In this work, the modified coprecipitation reaction was carried at a temperature of 80 °C and with the addition of glycine concentrations in the range of 0.06–0.60 mol to prepare iron oxide MNPs of different sizes. The optimisation of synthesis parameters allowed for production of iron oxide MNPs with controllable averaged diameters in the range from 10.2 ± 0.3 to 7.2 ± 0.5 nm and high crystallinity confirmed by the proximity of particle and crystal sizes, and relatively high values of saturation magnetisation. Magnetic properties were deeply studied by SQUID magnetometry and Mössbauer spectroscopy. Analysis of the parameters of the Mössbauer spectra of the synthesized iron oxide MNPs as well as the distribution functions of the effective magnetic fields on the iron nuclei $P(\mu_0 H_{eff})$ showed that in the MNPs investigated there exists a surface layer whose magnetic structure differs from that of the particle interior. The effective magnetic fields on the iron nuclei in the surface region are significantly lower than those on the iron nuclei in the core of the particle. The reasons for the formation of such a layer are analyzed. The magnitude of the $\mu_0 H_{eff}$ decrease agrees with theoretical estimates made within the framework of the theory of molecular orbitals.
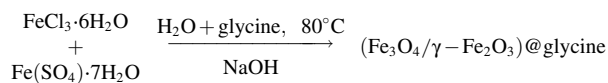
2. Materials and methods

2.1. Reagents

Iron (II) sulfate hydrate, $FeSO_4 \cdot 7H_2O$, iron (III) chloride hydrate, $FeCl_3 \cdot 6H_2O$ (Neva reactive Co., Russia), Glycine with a purity of 97% and sodium hydroxide (Neva reactive Co., Russia) were used. Ethanol (C_2H_5OOH) > 99% was utilized for washing the particles. Deionized water was used during the entire process for solution preparation. All purchased materials were used as received. All syntheses were performed under oxygen-free conditions.

2.2. Synthesis of glycine coated MNPs

Five samples of iron oxide MNPs (Fe_3O_4/γ-Fe_2O_3) were prepared by coprecipitation in the presence of different concentrations of glycine (0.06, 0.10, 0.15, 0.30 and 0.60 mol/L). All samples of MNPs were labelled according to the glycine content used in synthesis (G0.06, G0.10, G0.15, G0.30 and G0.60).

In a typical experiment (for example, for the G0.06 sample), 0.1 mol $FeSO_4 \cdot 7H_2O$ and 0.2 mol $FeCl_3 \cdot 6H_2O$ were dissolved in 50 mL degassed deionized water and added into a 100 mL flask, which was immersed in a room temperature water bath. Then the glycine was added to set the concentration of 0.06 mol/L in the reaction solution over the duration of the reaction. 3 mol of NaOH was dissolved in 20 mL degassed deionized water. The reaction solution was mechanically stirred at 800 rpm while heating up to 80 °C. After reaching a temperature of 80 °C, NaOH was added dropwise to the mixture, stirring was continued for 2 h. At the end of this reaction time, the solution was decanted, allowing the particles to be washed with ethanol and centrifuged at 2900 rpm for 10 min. This procedure was repeated twice, then the particles were separated and dried overnight at 70 °C. The schematic representation of synthesis route to produce glycine-functionalised MNPs is:

$$\begin{array}{c} FeCl_3 \cdot 6H_2O \\ + \\ Fe(SO_4) \cdot 7H_2O \end{array} \xrightarrow[\text{NaOH}]{H_2O + \text{glycine}, \ 80°C} (Fe_3O_4/\gamma - Fe_2O_3)@\text{glycine}$$

2.3. Morphostructural characterisation

X-ray diffraction (XRD) studies were performed with a DRON-3 diffractometer using Cu Kα with graphite monochromator ($\lambda = 1.54177$ Å) in the 2θ geometry in a range of 10–80 degrees. Rietveld analysis was performed on the XRD data using the software developed by Shelekhov and Sviridova [38]. The instrumental broadening was measured using a germanium powder sample without physical broadening. The lattice parameter precision was 0.008 Å.

The morphology of the samples was studied with a transmission electron microscope (TEM, Hitachi TM3000 with X flash 430 H detector, Bruker; HT7700, Hitachi) operated at 200 kV. The powders were first dispersed in n-hexane and placed in an ultrasonic treatment for about 10 min. A few drops of the suspension were placed on a carbon-coated copper grid and left to dry in the air. Particle size distribution was determined by analysis of TEM micrographs, fitted with a lognormal distribution:

$$P = \frac{A}{d\sigma\sqrt{2\pi}} \exp\left[-\frac{\ln^2\left(\frac{d}{\langle d_{TEM} \rangle}\right)}{2\sigma^2} \right], \tag{1}$$

where A is the area of the peak, d_{TEM} is the median value of the variable d and σ is the standard deviation. The particles size distribution was estimated by calculation of about two hundred particles from several images.

2.4. Thermal analysis

Simultaneous Thermal Analysis (STA) was performed on a NETZSCH STA 449 C instrument with a Quadrupole Mass Spectrometer (QMS) 403 C (mass control $m/z = 18, 28, 30, 32, 40, 44, 46$). All analyses were performed under a dynamic atmosphere (20% O_2–Ar) with a flow rate of 63 cm^3/min in a platinum crucible with a perforated lid. The temperature was first stabilized for 30 min at 40 °C, then simultaneously Thermogravimetric (TG) and Differential Scanning Calorimetry (DSC) analyses were performed in a heating process with the rate of 15°/min to 1000 °C.

2.5. Magnetic properties

Magnetic properties of the nanoparticles were investigated using a vibrating sample magnetometer of a Quantum Design Physical Property Measurement System (PPMS 9 T) in the field range up to 9 T. The magnetisation was normalised by the mass of the sample considering the organic content known from TG analysis. M vs T curves were measured in a magnetic field of 10 mT for the sample after cooling in zero field (ZFC curve) and cooling in a non-zero magnetic field (FC curve) [39]. Specifically, in the ZFC protocol, the sample was cooled down to 4.2 K in the absence of a magnetic field, then the measuring magnetic field was applied and the magnetization was recorded during heating from 4.2 K to 300 K. In the FC protocol, the sample was cooled in the magnetic field of 10 mT and then the magnetization was recorded during the heating in the same measuring field.

2.6. Mössbauer spectroscopy

The state of the Fe atoms in the samples was investigated using a Mössbauer spectrometer operating in constant acceleration mode with a triangular form of change in the Doppler velocity of the source relative to the absorber. A ^{57}Co isotope in Rh matrix was used as a source of γ-radiation. The measurements were performed in the geometry of transmission of γ-rays through the sample at 300 K or 80 K. The velocity was calibrated using a metal foil absorber made of α-Fe. Isomeric shift (δ) values were determined relative to the α-Fe metal foil at 300 K. The experimental Mössbauer spectra (MS) were mathematically processed using a program using the least-squares method and the Lorentzian form of spectral lines, as well as the method of decoding spectra by restoring the distributions of hyperfine interactions (HFI) parameters, within the framework of the magnetic particle size distribution model implemented in the SpectrRelax program [40]. Information on the phase composition was obtained by analyzing the parameters of hyperfine interactions obtained from experimental MS.

3. Results and discussions

3.1. Morphostructural characterisation

X-Ray Diffraction (XRD) data of all prepared samples present a typical pattern of a cubic spinel ferrite with no impurities (Fig. 1). Phase distinguishing between maghemite and magnetite especially for nanostructural materials is a complicated task due to similar spinel structures with similar positions and intensities of peaks. The typical value of lattice parameter (a) for maghemite is 0.834 nm and for magnetite is 0.839 nm [41]. The observed value of lattice constant laying between both and it slightly increases for the sample prepared with the minimal concentration (0.06 mol) of glycine (Table 1). The size of crystallites (d_{XRD}) for samples G0.06–0.15 are around 9 nm and equivalent within the frame of experimental error. For samples G0.30 and G0.60, the d_{XRD} gradually decreases to 8.3 ± 0.5 and 6.8 ± 0.5 nm respectively.

According to the TEM investigation, particles have nonhomogeneous rectangular/spherical shapes (Fig. 2(a)). Resultant size distributions fitted with the lognormal function are shown in Fig. 2(b). Average
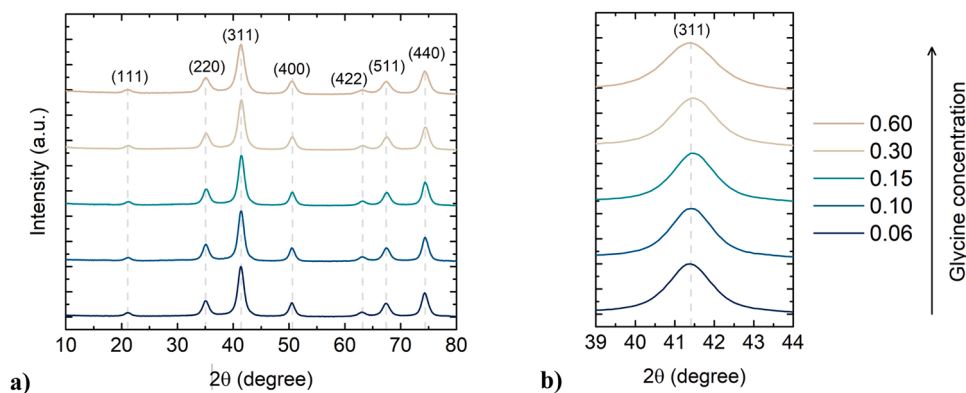
Fig. 1. (a) XRD patterns of iron oxide MNPs prepared in the presence of different concentrations of glycine; (b) enlargement of the strongest (311) reflection: one can observe a slight peak broadening and preserving its position with an increase in glycine concentration.

Table 1
Results of XRD and TEM analysis of MNP samples prepared at different glycine concentrations: lattice parameter (a), crystallite size (d_{XRD}), median particle size (d_{TEM}) and standard deviation of the log of the distribution (σ).

Sample	Glycine concentration (mol/L)	a (nm)	d_{XRD} (nm)	d_{TEM} (nm)	σ
G0.06	0.06	0.8368	8.8 ± 0.5	10.2 ± 0.3	0.31 ± 0.03
G0.10	0.10	0.8360	9.4 ± 0.5	10.1 ± 0.2	0.20 ± 0.02
G0.15	0.15	0.8361	9.3 ± 0.5	9.7 ± 0.2	0.23 ± 0.02
G0.30	0.30	0.8361	8.3 ± 0.5	8.1 ± 0.3	0.33 ± 0.03
G0.60	0.60	0.8362	6.8 ± 0.5	7.2 ± 0.5	0.35 ± 0.07

particle sizes (d_{TEM}) decrease with the increase of glycine concentration in agreement with decreased size of crystallites d_{XRD} (Table 1). The d_{TEM} was slightly larger than the d_{XRD} for bigger particles and almost equal for smaller ones, which confirms the good crystal nature of particles. Particle size with the increase of glycine content decreases slowly in comparison to a similar system, where instead of glycine, different concentrations of citric acid were added before precipitation of iron oxide MNPs [42].

3.2. Thermal properties

According to STA three distinct processes are observed under heating of the samples in the oxidative atmosphere (Fig. 3(a,b)):

- 40–150 °C: mass loss due to endothermic elimination of water;
- 150–600 °C: mass loss with the simultaneous exothermic process of $H_2O + CO_2$ formation;
- 580–670 °C: a pronounced exothermal effect without a noticeable change in mass.

Released compounds were determined by QMS, namely two ion currents with the intensity of m/z equals to 18 (H_2O) and 44 (CO_2) (data not shown). Thus, during the heating, first, the absorbed water evaporates and then the glycine oxidizes. According to TG, the mass is almost constant after 800 °C, thus the $(100 - \Delta m_{40-800})$ value (%) (Table 2) can be considered as inorganic content with some possible additional error due to oxidation of magnetite to maghemite (if the first was present). The process of magnetite oxidation should be accompanied by a mass gain of 3.45% ($2 \times Fe_3O_4 + \frac{1}{2} \times O_2 = 3 \times Fe_2O_3$), that however was not detected due to water and organic content elimination processes
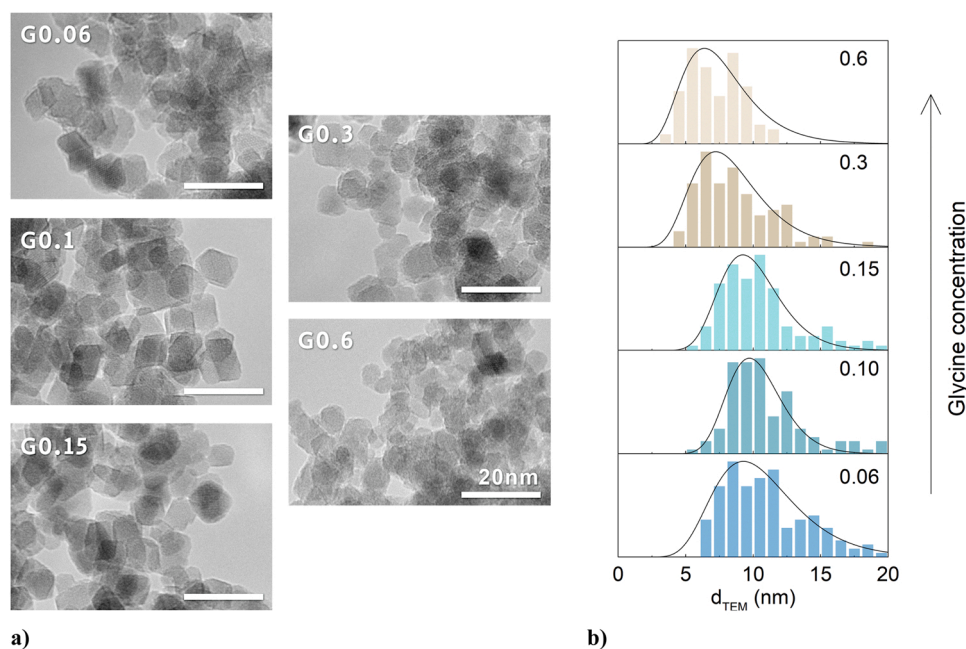
Fig. 2. (a) TEM images of G0.06–G0.60 samples (scale bar of 20 nm is the same for all images); (b) hystograms and results of log-normal fit of particle size distribution.
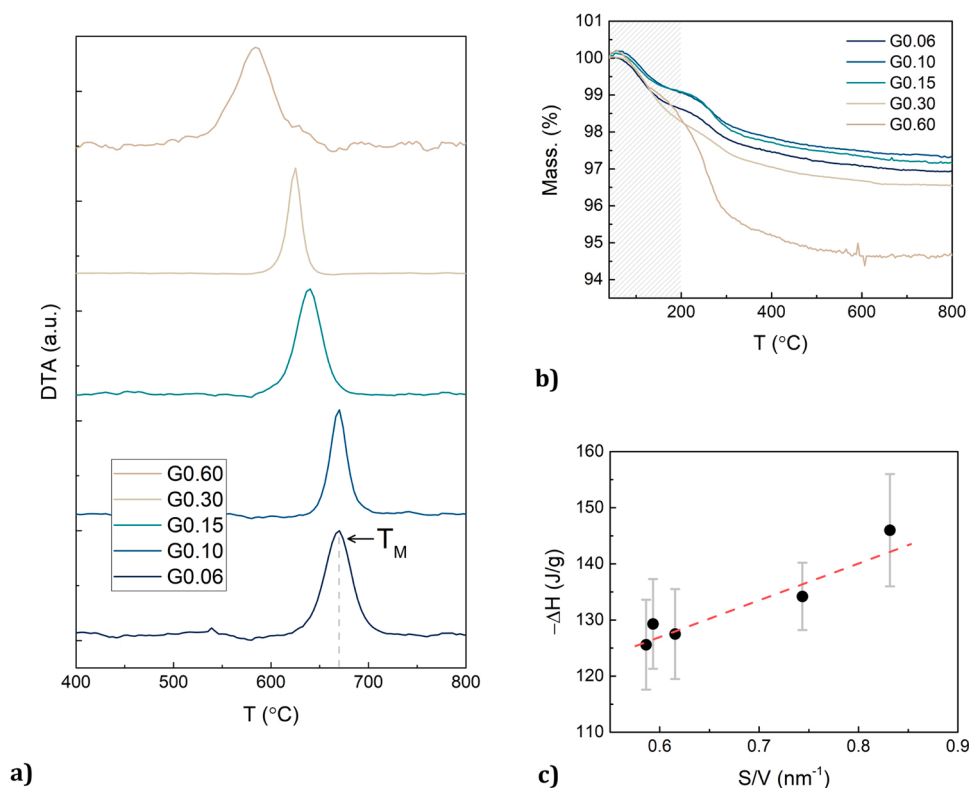
Fig. 3. (a) Differential scanning calorimetry and (b) thermogravimetric DSC curves for thermal conversion of G0.06–G0.60 samples (20%O_2 – Ar, $\beta = 15°$/min); (c) enthalpy associated with phase transition at T_M as a function of surface-to-volume ratio (S/V) of MNPs.

occurring at the same temperature region [43]. Pronounced exothermal effect with peaks at T_M without a noticeable change in mass (or with a very weak change) can be attributed to the phase transition of maghemite to hematite [43]. Comparing Δm_{40-800}, one can note that it decreases with the increase in the particle size, and it is almost constant in the frame of errors for samples G0.06, G0.10 and G0.15 of the same sizes. The increase of Δm_{40-800} with the concentration of the glycine added is most probably a result of combined action of enhanced glycine sorption from concentrated solutions and expected particle`s surface growth in the series of G0.06–G0.60. The shift of the T_M value reflects changes in the thermal stability of the oxide phase. It was shown that nanocrystalline γ-Fe_2O_3 has a higher transition temperature than the coarse-grained counterpart [44]. In our case, we have an opposite trend: the T_M value is shifted for the smaller particles to the lower temperatures, and it can be related to the changes of the enthalpy, associated with phase transition at T_M (Fig. 3b). To better explain this result, further studies are needed.

3.3. Magnetic properties

The magnetic properties of all samples were studied with the vibrating sample magnetometer of a Quantum Design Physical Property Measurement System (PPMS 9 T) (Fig. 4). In all cases, the M_S at 4.2 K

Table 2
The results of STA for G0.06–G0.6 samples: mass loss at 200 °C (Δm_{40-200}) and at 800 °C (Δm_{40-800}), the position of the exothermal peak (T_M) and enthalpy associated with phase transition at T_M.

Sample	Δm_{40-200}, %	Δm_{40-800}, %	T_M, °C	$-\Delta H$, J/g
G0.06	1.4 ± 0.1	3.1 ± 0.1	669 ± 1	126 ± 8
G0.10	1.0 ± 0.1	3.0 ± 0.1	639 ± 1	129 ± 8
G0.15	1.1 ± 0.1	2.9 ± 0.1	669 ± 1	128 ± 8
G0.30	1.8 ± 0.1	3.5 ± 0.1	625 ± 1	134 ± 6
G0.60	1.8 ± 0.2	5.5 ± 0.2	581 ± 1	146 ± 10

(Table 3) is smaller than that of bulk Fe_3O_4 (92 Am^2/kg) or γ-Fe_2O_3 (83 Am^2/kg) [45,46]. Nevertheless, the reduction in M_S values for small crystals is expected, due to the surface spin disorder [22,23]. The lowest M_S value (64 ± 3 Am^2/kg at 4.2 K) was found in the sample G0.60, while for the rest of the samples, this value is almost equal within the confidence interval. The coercivity is also almost unaltered for the whole set of samples, except for the sample G0.60. Obtained M_S and $\mu_0 H_C$ values are in accordance with literature data for magnetic iron oxide nanoparticles in the studied size range [47–49]. At 300 K, all M-H curves exhibit superparamagnetic character with no observable coercivity and remanence (Fig. 4(b)). The M_S value measured at 300 K was higher than the value of 27 Am^2/kg found in smaller iron oxide MNPs of smaller size prepared by similar one-pot approach in the presence of glycine [26].

Temperature dependence of magnetisation measured for ZFC and FC samples represents a typical bifurcating curve for superparamagnetic particles (Fig. 5a). The peak value of the ZFC curve (T_{max}) shifts toward the lower temperatures for samples prepared in the presence of the higher glycine content. The blocking temperature (T_B) is defined by the transition from the blocked to the superparamagnetic state of a 50% volume fraction of particles [50,51]. According to refs.[50,51], the blocking temperature can be found from the derivative of the difference of ZFC and FC magnetization curves d($M_{ZFC} - M_{FC}$)/dT (Fig. 5b). The d($M_{ZFC} - M_{FC}$)/dT derivative represents the distribution of blocking temperatures. The mean T_B value can be defined as a temperature where the integral value reaches 50% (alternatively, as the inflection point of the ZFC curve or a maximum of d($M_{ZFC} - M_{FC}$)/dT). Although d($M_{ZFC} - M_{FC}$)/dT does not reach zero at low temperatures (probably due to interparticle interactions or surface spin freezing), the trend of T_B agrees with the trend of T_{max}. Both T_{max} and T_B values decrease with the decrease in particle size (or increase in glycine content). Linear dependence of T_B versus particle volume (V ~ d_{TEM}^3) in Fig. 5c is since T_B ~ KV, where K is the anisotropy constant. Thus, T_B is proportional to the particle size if K does not depend on it. T_{max} is related to T_B according to equation $\beta \approx T_{max}/T_B$ [52]. The shift of T_{max} from T_B and, as the
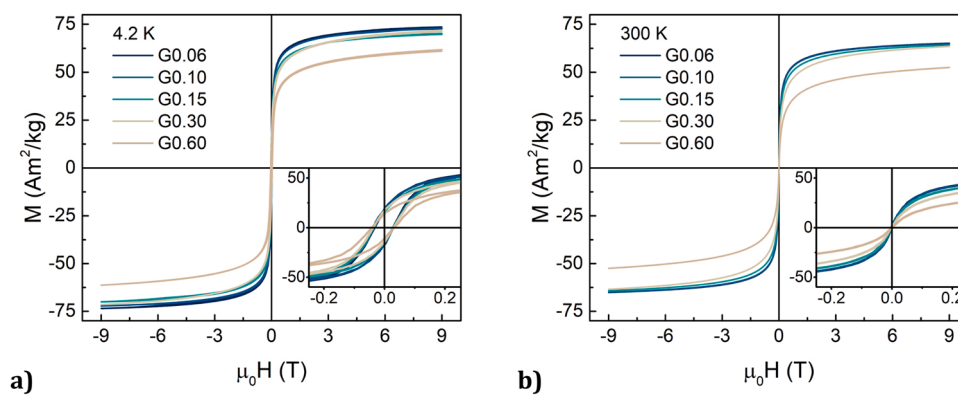
Fig. 4. M-H curves measured at (a) 4.2 K and (b) 300 K. Insets: enlargement of a low-field region.

Table 3
Magnetic properties of samples: the saturation magnetization (M_S), the coercive field ($\mu_0 H_C$), the maximum of M_{ZFC} (T_{max}) and the blocking temperature (T_B).

Sample	M_S, Am^2/kg		$\mu_0 H_C$, mT	T_{max},	T_B,	β
	(4.2 K)	(300 K)	(4.2 K)	K	K	(T_{max}/T_B)
G0.06	73 ± 4	69 ± 4	30 ± 1	227 ± 2	77 ± 2	3.0
G0.10	75 ± 4	69 ± 4	34 ± 1	220 ± 2	76 ± 2	2.9
G0.15	70 ± 4	68 ± 4	31 ± 1	199 ± 2	71 ± 2	2.8
G0.30	74 ± 4	69 ± 4	34 ± 1	169 ± 2	63 ± 2	2.7
G0.60	64 ± 3	59 ± 3	37 ± 1	142 ± 2	58 ± 2	2.4

consequence, the value of the β coefficient, is due to particle size distribution. In our case, the value of β gradually decreases from the value of 3.0 for the G0.06 sample to 2.4 for the G0.60 sample.

3.4. Mössbauer spectroscopy

Iron oxides have very rich chemistry and there are several magnetic and non-magnetic forms (Fe_3O_4, γ-Fe_2O_3, α-Fe_2O_3, and others) stable at ambient conditions. Distinguishing magnetic oxides, Fe_3O_4 and γ-Fe_2O_3 is practically impossible by laboratory X-ray diffraction techniques because the lattice constants of these oxides are so close. The same is true of the magnetic properties of those oxides by standard magnetometry methods. Mössbauer spectroscopy is a very sensitive method that provides information about Fe ions occupying non-equivalent lattice positions because the hyperfine field parameters for Fe are located in different sublattices [53–56]. Utilizing Mössbauer spectroscopy it is possible to determine the phase composition and determine the content of various iron oxides in the studied material, which is not possible by other techniques.

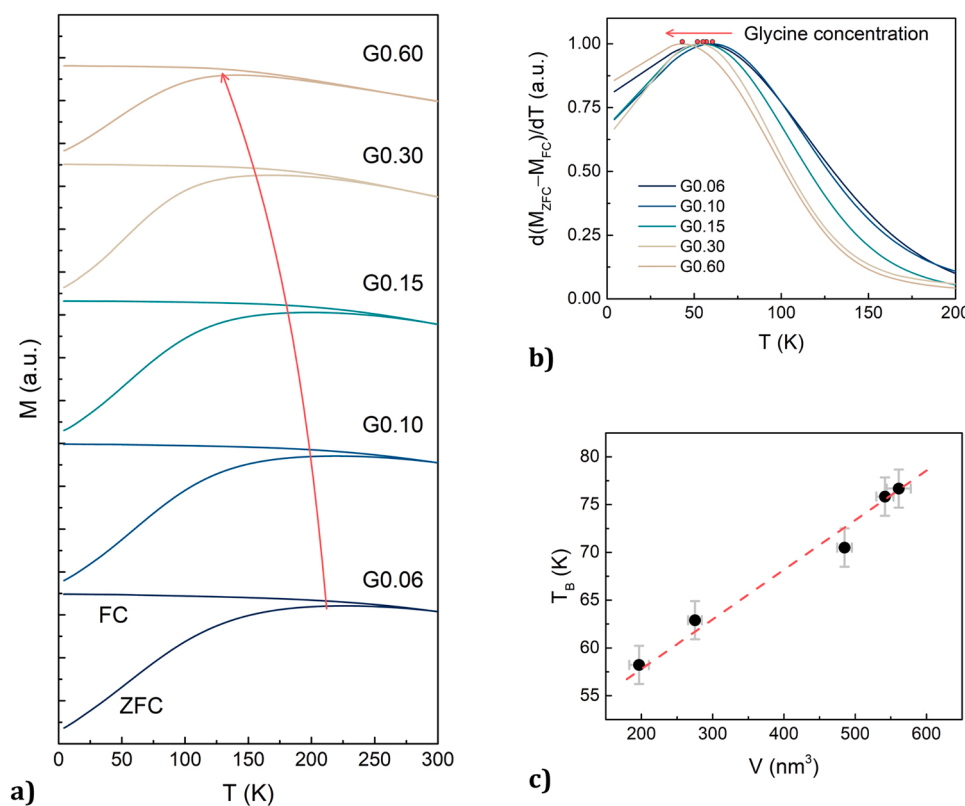The experimental Mössbauer spectra (MS) of G0.10, G0.3 and G0.6

Fig. 5. (a) ZFC and FC curves measured in a measuring field of 10 mT (arrow indicates the temperature of the maximum of the ZFC curve); (b) energy barrier distribution $d(M_{ZFC} - M_{FC})/dT$ plotted versus temperature (dots indicate its maximum); (c) blocking temperature as a function of particle volume.

(samples with gradually changed size) obtained at 300 K and 80 K are shown in Fig. 6(a,c), respectively. The experimental values are shown in Fig. 6(a,c) by dots, whereas the model spectra obtained by mathematical processing of the experimental MS using the SpectrRelax program [40] are shown by solid lines. The good agreement of the models used with the experimental G0.15, G0.3 and G0.6 MS is confirmed by the minimum values of the difference between the model and experimental

values shown above each spectrum, as well as the values of $\chi 2$ being in the range 1.0–1.2. The distribution functions of the effective magnetic fields $P(\mu_0 H_{eff})$ obtained at 300 K and 80 K with a specialized program [40] are shown in Fig. 6(b,d), respectively.

The MS (Fig. 6(a,c)) show broad Zeeman splitting lines, and doublets are present in the zero velocity region. The presence of doublets can be explained by the presence of a fraction of superparamagnetic particles.
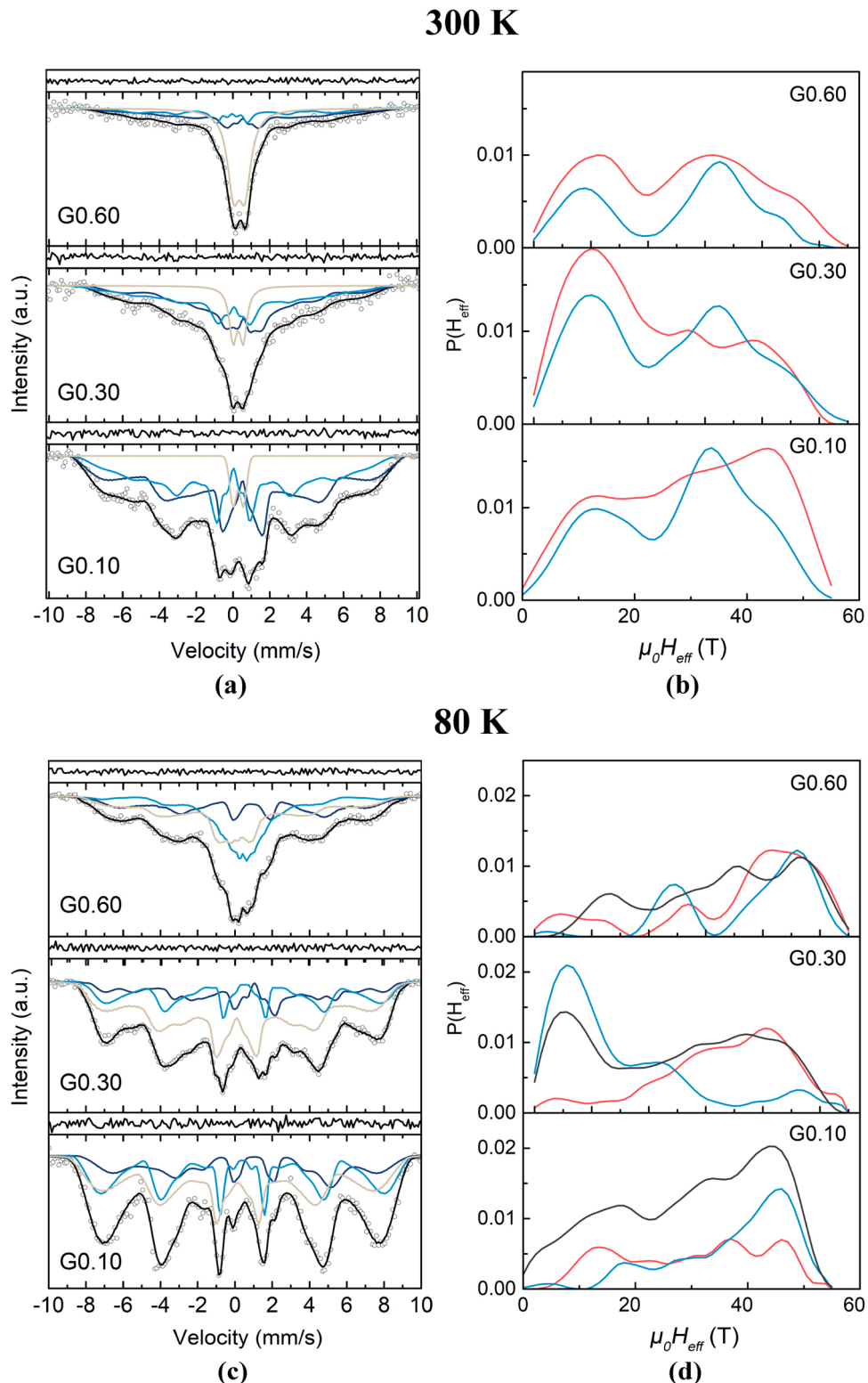

Fig. 6. Mössbauer spectra (a,c) and corresponding hyperfine field distribution (b,d) for samples G0.10, G0.30 and G0.60 at 300 K (a,b) and 80 K (c,d).

The observed experimental MS in Fig. 6 are similar to those of magnetite obtained in [55–57]. The hyperfine interaction (HFI) parameters, namely, isomer shift (δ), quadrupole splitting (ε), and effective magnetic field ($\mu_0 H_{eff}$), presented in Table 4 were calculated and analyzed from the positions of lines in the MS.

3.5. Analysis of Mössbauer spectra recorded at 300 K

In magnetite (Fe_3O_4), Fe^{2+} ions occupy two non-equivalent tetrahedral (A-site) and octahedral (B-site) crystallographic positions [26], with Fe^{2+} ions occupying half of the B-lattice and Fe^{3+} ions equally distributed over the A-positions and in the remaining half of the B-positions. Therefore, there should be three Zeeman sextets on the MS of magnetite due to the contributions of iron ions at the crystallographic A and B positions. However, in magnetite crystals, there is a Verwey phase transition (T_v) at 119 K accompanied by a change in the electronic state of iron cations in the B-positions of the crystal lattice [58]. At temperatures above T_v, Fe^{3+} and Fe^{2+} occupying B-positions are in the state of electronic exchange and can be referred as $Fe^{2.5+}$ cations, which should correspond to one partial Zeeman sextet [53,54,59]. The other sextets are formed by Fe ions in the A-position. Therefore, a model consisting of two partial Zeeman sextets belonging to the fraction of magnetite

particles with magnetic ordering and a doublet belonging to particles in the paramagnetic phase was used in the mathematical processing of the MS. The large width of spectral lines ($\Gamma = 0.7$ mm/s) observed on the MS of the studied samples indicates the particle size distribution.

The Fe ions in the tetrahedral positions have a typical isomer shift of around 0.427 mm/s and a small quadrupole splitting, characteristic of tetrahedrally coordinated Fe^{3+}. The hyperfine field is 32.5 T. The second component with more than double the area has an IS of 0.427 mm/s, a minor quadrupole splitting, and an effective magnetic field of 36 T. This sextet belongs to iron ions in octahedral coordinations. For Fe_3O_4 bulk (not shown here) the HFI parameters obtained at room temperature are: for A-position iron ions $\delta = 0.29(1)$ mm/s, $\mu_0 H_{eff} \approx 48$ T, for B-position $\delta = 0.61(1)$ mm/s, $\mu_0 H_{eff} \approx 46$ T.

3.6. Analysis of Mössbauer spectra recorded at 80 K

It should be noted that the MS of magnetite MNPs at temperatures below T_v change significantly [58,60–63], the interpretation of the MS becomes significantly more complicated and, therefore, the interpretations of the MS are very contradictory. The results of low-temperature Mössbauer studies [58,60–62,64,65], along with the data of nuclear magnetic resonance [62,64] give evidence against the

Table 4

HFI parameters calculated from Mössbauer spectra of MNPs at 300 K and 80 K (δ – isomer shift, ε – quadrupole splitting, $\mu_0 H_{eff}$ – effective magnetic field, S – area of sextet/doublet).

Sample	Comp.		G, mm/s	δ, mm/s	ε, mm/s	$\mu_0 H_{eff}$, T	S, %
300 K							
G0.60	Fe_3O_4	$Fe^{2,5+}$	0.210±0.070	0.493±0.080	−0.039±0.080	31.6±4.0	34±13
		Fe^{3+}	0.210±0.070	0.022±0.120	0.077±0.110	32.6±1.0	19±10
	doublet		0.774±0.090	0.343±0.021	0.311±0.013	—	47±11
G0.30	Fe_3O_4	$Fe^{2,5+}$	0.301±0.170	0.495±0.130	−0.081±0.110	10.0±1.6	47±14
		Fe^{3+}	0.301±0.170	0.011±0.110	−0.041±0.090	10.2±2.0	40±16
	doublet		0.476±0.100	0.273±0.040	0.274±0.016	—	13±5
G0.10	Fe_3O_4	$Fe^{2,5+}$	0.210±0.040	0.395±0.050	−0.119±0.050	44.2±1.1	55±10
		Fe^{3+}	0.210±0.040	0.061±0.070	0.042±0.060	33.8±0.5	40±10
	doublet		0.431±0.070	0.281±0.040	0.274±0.020	—	5±2
80 K							
G0.60	Fe_3O_4	Fe_1^{3+}	0.200±0.130	0.412±0.070	−0.042±0.080	5.4±1.1	32±21
		Fe_2^{3+}	0.200±0.240	0.108±0.090	0.117±0.080	5.9±1.6	42±15
		Fe^{2+}	0.200±0.240	0.701±0.090	−0.243±0.090	40.3±1.8	27±14
G0.30	Fe_3O_4	Fe_1^{3+}	0.220±0.080	0.513±0.080	−0.030±0.070	46.5±0.9	23±19
		Fe_2^{3+}	0.220±0.080	0.154±0.040	0.044±0.035	43.5±1.9	58±14
		Fe^{2+}	0.220±0.080	0.801±0.130	−0.273±0.130	37.2±1.4	20±12
G0.10	Fe_3O_4	Fe_1^{3+}	0.246±0.320	0.428±0.100	0.000±0.070	47.2±0.8	32±33
		Fe_2^{3+}	0.248±0.340	0.183±0.120	0.007±0.110	44.7±1.6	49±31
		Fe^{2+}	0.249±0.600	0.800±0.190	−0.241±0.190	43.7±1.7	20±17

validity of the Verwey description, which implies the existence of three components with the same intensity, one for each of the three types of atoms (tetrahedral Fe^{3+}, two octahedral Fe^{2+} and Fe^{3+}). Thus, the MS of magnetite at low temperatures in [66] was described using one Zeeman sextet for iron ions in A-sites and five magnetic components for Fe ions in octahedral B-sites. In [60,61] it was concluded that the MS below T_v is better described by the five components. One component corresponds to the tetrahedral A-position of Fe ions, and the other four to the two non-equivalent octahedral B-positions of Fe^{2+} and Fe^{3+} ions. In [63,64], based on the 24 sextets, it was concluded that the 24 positions of iron ions are naturally divided into four groups: $8 \times Fe^{3+}(A)$, $8 \times Fe^{3+}$-like (B) positions, $5 \times Fe^{2+}$-like (B) and $3 \times Fe^{2+}$-like (B) positions of Fe ions and the MS approximation at temperatures below T_v was performed using the four Zeeman components. Thus, the question of charge ordering of the low-temperature phase has been to the subject of many studies, but an adequate model for the interpretation of the MS of magnetite has not yet been found. The difficulties in interpreting the data are caused by the fact that direct structural information on the properties of the dielectric state of magnetite crystals was practically unavailable because of their twinning. The development of synchrotron diffraction methods at high γ-radiation energy (70 keV) allow for obtaining precision structural data from a Fe_3O_4 crystals of 40 μm in size [65]. Based on the results obtained, it can be argued that the predominant phase in all studied samples is magnetite.

Based on the above, the MS obtained at 80 K (Fig. 6(c,d)) were processed using the SpectrRelax program [40] using different models, namely, consisting of one doublet and five, four, or three Zeeman sextets. As a result, it was found that the experimental MS are best described as a superposition of three Zeeman sextets, as confirmed by the minimum difference values between the model and experimental values as well as the χ2 values that are within 1.0–1.2. The obtained HFI parameters are shown in Table 4.

3.7. μ_0H_{eff} distribution functions

The lack of clear resolution of the sextets on the MS of the studied MNPs significantly complicates obtaining a clear physical fitting model. Therefore, the distribution functions of the effective magnetic fields P (μ_0H_{eff}) are presented in Fig. 6(b,d). It should be noted that the best agreement with the experimental spectra at 300 K was obtained using two μ_0H_{eff} distribution functions, whereas three μ_0H_{eff} distributions were used for MS at 80 K. As can be seen from Fig. 6(b,d), the P(μ_0H_{eff}) functions obtained both at 300 K and 80 K differ from the P(μ_0H_{eff}) function we obtained for the bulk magnetite (not shown here), where only the maxima corresponding to the 49 and 46 T fields are observed, similar to those observed, for example, in [67].

The P(μ_0H_{eff}) functions obtained from MS at 300 K (Fig. 6(b)) show maximums in two μ_0H_{eff} regions, namely, from 5 T to 20 T and from 20 T to 55 T. For the MNPs with minimal glycine content among those studied (G0.10 sample), the distribution functions are smoothed. Increasing the glycine concentration apparently leads to an increase in the isolation of the particles from each other, a decrease in the magnetic interaction between them, and an enhancement of the superparamagnetic contribution.

At 80 K, the MS were reconstructed using three μ_0H_{eff} distributions, which show a greater number of maxima (Fig. 6(d)), the smaller the area under the maximum the lower the corresponding μ_0H_{eff}. Two μ_0H_{eff} distributions of these three behave almost identically under the synthesis conditions used and have area ratios of approximately 2:1. The δ values of the former are about 0.4–0.5 mm/s and of the latter are 0.1–0.2 mm/s. These distributions can be attributed to the A and B sublattices of magnetite.

Let us consider the reasons for the differences in the μ_0H_{eff} distribution functions for MNPs and bulk magnetite. First, the presence of a surface leads to a decrease in the number of exchange bonds of iron ions located on the surface, and in the case of MNPs the contribution to the

MS of the Fe nuclei, which have fewer exchange bonds, becomes significant, i.e. the "surface factor" becomes significant in terms of the magnetic structure of the particle. In [68], using the method of molecular orbitals, it was found that the contributions to μ_0H_{eff} from each of the indirect exchange bonds for the Fe^{3+} ions in the spinel structure for octa- and tetrahedral positions are 0.8 and 1.2 T, respectively. Since the ions in the A-sites have 12 iron ions in the B- sites in the nearest cationic environment, and the iron ion in the B- sites has 6 iron ions in the A-sites, the absence of half of the bonds due to the surface should result in a decrease of μ_0H_{eff} by several Tesla, as was found in the literature [53,54, 68]. On this basis, the maximum in the region of 48 T in the P(μ_0H_{eff}) distributions (Fig. 6(d)) can be attributed to iron ions located in the particle volume. Iron ions located on the surface of the MNPs do not have half of the nearest magnetic neighbors, which leads to a decrease in μ_0H_{eff}, and, therefore, there is a maximum in the P(μ_0H_{eff}) function in the region of 35 T.

Another reason for the lowering of μ_0H_{eff} may be the formation of a canted spin structure in the surface layer of the MNPs (see, [69,70] and references therein). It is known that ferromagnetic nanoparticles exhibit a non-collinear spin structure, but the location of these disordered spin moments on the surface or in the entire volume of the MNPs is discussed in [69,70]. The real spin structure is known to be more diverse and more complex than expected in the Yafet–Kittel model [71]. It has been shown that a canted state of magnetic spin moments can be observed both in one magnetic sublattice and in both cationic sites [72–74].

The behavior of the third distribution function μ_0H_{eff} (Fig. 6(d)) can also be explained by a core-shell type structure of the synthesized particles in which the core is magnetite surrounded by a shell of an oxidized layer structurally similar to maghemite [45,49].

In the interpretation of MS obtained at 80 K, the doublets were not used, whereas in the analysis of 300 K MS the calculations without doublet lines belonging to the superparamagnetic state of the particles led to large deviations of the model spectra from the experimental ones.

3.8. Particle size estimation

Mössbauer spectroscopy is extremely sensitive to the particle size and allows one to indirectly determine sizes of investigated MNPs. Thus, in the case of MNPs with sizes of several nm, the magnetization vector relaxation rate is greater than the Larmor precession rate of the nuclear spin. As a result, the mean value of HFI becomes zero and a quadrupole doublet or singlet is observed on the MS. If the particle size is between 6 nm and 10 nm, the MS consists of broad lines of Zeeman splitting, against which a quadrupole doublet or singlet is observed. As the size of the investigated MNPs increases up to 10–12 nm, the MS are substantially transformed and consist only of Zeeman sextets with sufficiently wide lines compared to the native line widths for Fe^{57}. This is because in MNPs larger than 10 nm, the precession frequency of the magnetization vector decreases and keeps its direction for a time longer than the time of the Larmor precession. In this case, Zeeman sextets with large line widths of the static hyperfine magnetic structure are observed in the MS. Increasing the particle size to 20 nm causes the Zeeman sextets belonging to different phases or components to resolve.

In works [53–55,75–80] and references therein, the iron oxide MNPs with sizes from 3 to 20 nm were studied by Mössbauer spectroscopy. It was shown that if the dimensions of iron oxide MNPs are 7 nm or smaller, only doublets can be observed on MS at 300 K [55,75,76,78]. When iron oxide MNPs are larger than 10 nm, the MS consist of a Zeeman sextet with large line widths (e.g., [78]). Analysis and comparison of the MS obtained by us with those published in the literature allow us to conclude that the studied particles are in the size range of 7–10 nm and the median size decreases with the increase in glycine content, which agrees with observations obtained with other techniques.

4. Conclusions

In conclusion, in the present paper, we report on the systematic study of the magnetic and structural properties, phase composition, and magnetic structure of iron oxide MNPs prepared with a modified one-step coprecipitation method in the presence of glycine of different concentrations. A range of glycine concentrations of 0.06–0.60 mol was used, and we observe a fall in median particle size from 10.2 ± 0.3 nm at the lowest concentrations of 0.06 mol, to 7.2 ± 0.5 nm at the highest concentration of 0.60 mol. This change in size has a notable effect on their magnetic properties, with blocking temperature falling from 77 ± 2 K at the lowest concentration to 58 ± 2 K at the highest. Magnetic properties of obtained particles start degrading when the concentration of glycine added before precipitation exceeds 0.3 mol: the saturation magnetisation drops significantly due to the large fraction of canted spins at the surface. Owing to the selection of optimal synthesis parameters, the saturation magnetization prepared MNPs achieved significantly higher values compared to those previously reported for nanoparticles prepared in a similar approach at lower temperature and with a different base. This is also confirmed via Mössbauer spectroscopy by lowering of the effective magnetic field. Also, at the Mössbauer time scale, the contribution of superparamagnetic relaxation increases with the increase in glycine concentration due to the reduction of particle sizes and distances between particles. The high magnetic properties were related to the high crystallinity of the nanoparticles, as evidenced by the proximity of particle sizes and coherent X-ray scattering regions, and distinguishable by TEM crystalline facets of the nanoparticles. We believe that the proposed method for the fabrication of functionally coated nanoparticles in a one-step process with large reaction yields and cheap reagents is promising for a number of applications, such as biomedicine or water purification.

Funding

CRediT authorship contribution statement

Omelyanchik: Data curation, Writing – original draft preparation, Visualization, Conceptualization, Methodology. **A.S. Kamzin**: Supervision, Data curation, Writing – original draft preparation, Investigation, Conceptualization. **A.A. Valiullin**: Methodology, Investigation (Mössbauer spectroscopy). **V.G. Semenov**: Methodology, Investigation (Mössbauer spectroscopy). **S.N. Vereshchagin**: Investigation (TGA), Writing – original draft preparation. **M. Volochaev**: Investigation (TEM). **A. Dubrovskiy**: Investigation (SQUID magnetometry), Writing – original draft preparation. **T. Sviridova**: Investigation (XRD analysis). **I. Kozenkov**: Investigation (synthesis). **E. Dolan**: Writing – review & editing. **D. Peddis**: Supervision, Project administration, Formal analysis. **A. Sokolov**: Supervision, Project administration, Formal analysis. **V. Rodionova**: Supervision, Project administration, Formal analysis, Funding acquisition.

Declaration of Competing Interest

The authors declare that they have no known competing financial interests or personal relationships that could have appeared to influence the work reported in this paper.

References

[1] V.F. Cardoso, A. Francesko, C. Ribeiro, M. Bañobre-López, P. Martins, S. Lanceros-Mendez, Advances in magnetic nanoparticles for biomedical applications, Adv. Healthc. Mater. 7 (2018) 1–35, https://doi.org/10.1002/adhm.201700845.

[2] G. Song, M. Kenney, Y.-S. Chen, X. Zheng, Y. Deng, Z. Chen, S.X. Wang, S. S. Gambhir, H. Dai, J. Rao, Carbon-coated FeCo nanoparticles as sensitive magnetic-particle-imaging tracers with photothermal and magnetothermal properties, Nat. Biomed. Eng. 4 (2020) 325–334, https://doi.org/10.1038/s41551-019-0506-0.

[3] V. Socoliuc, D. Peddis, V.I. Petrenko, M.V. Avdeev, D. Susan-resiga, T. Szabó, R. Turcu, E. Tombácz, L. Vékás, Magnetic nanoparticle systems for nanomedicine — a materials science, Perspect. Magetochem. 6 (2019) 1–36, https://doi.org/10.3390/magnetochemistry6010002.

[4] M.U. Farooq, V. Novosad, E.A. Rozhkova, H. Wali, A. Ali, A.A. Fateh, P.B. Neogi, A. Neogi, Z. Wang, Gold nanoparticles-enabled efficient dual delivery of anticancer therapeutics to HeLa cells, Sci. Rep. 8 (2018) 2907, https://doi.org/10.1038/s41598-018-21331-y.

[5] P.M. Martins, A.C. Lima, S. Ribeiro, S. Lanceros-Mendez, P. Martins, Magnetic nanoparticles for biomedical applications: from the soul of the earth to the deep history of ourselves, ACS Appl. Bio Mater. 4 (2021) 5839–5870, https://doi.org/10.1021/acsabm.1c00440.

[6] L. Maldonado-Camargo, M. Unni, C. Rinaldi, Magnetic characterization of iron oxide nanoparticles for biomedical applications, Methods Mol. Biol. (2017) 47–71, https://doi.org/10.1007/978-1-4939-6840-4_4.

[7] K. Levada, S. Pshenichnikov, A. Omelyanchik, V. Rodionova, A. Nikitin, A. Savchenko, I. Schetinin, D. Zhukov, M. Abakumov, A. Majouga, M. Lunova, M. Jirsa, B. Smolková, M. Uzhytchak, A. Dejneka, O. Lunov, Progressive lysosomal membrane permeabilization induced by iron oxide nanoparticles drives hepatic cell autophagy and apoptosis, Nano Converg. (2020), https://doi.org/10.1186/s40580-020-00228-5.

[8] M.V. Tkachenko, A.S. Kamzin, Synthesis and properties of hybrid hydroxyapatite–ferrite (Fe3O4) particles for hyperthermia applications, Phys. Solid State 58 (2016) 763–770, https://doi.org/10.1134/S1063783416040260.

[9] A.S. Kamzin, A.A. Valiullin, H. Khurshid, Z. Nemati, H. Srikanth, M.H. Phan, Mössbauer studies of core-shell FeO/Fe3O4 nanoparticles, Phys. Solid State 60 (2018) 382–389, https://doi.org/10.1134/S1063783418020129.

[10] S. Waldvogel-Abramowski, G. Waeber, C. Gassner, A. Buser, B.M. Frey, B. Favrat, J. D. Tissot, Physiology of iron metabolism, Transfus. Med. Hemother. 41 (2014) 213–221, https://doi.org/10.1159/000362888.

[11] T. Vangijzegem, D. Stanicki, S. Laurent, Magnetic iron oxide nanoparticles for drug delivery: applications and characteristics, Expert Opin. Drug Deliv. 16 (2019) 69–78, https://doi.org/10.1080/17425247.2019.1554647.

[12] M.J. Mitchell, M.M. Billingsley, R.M. Haley, M.E. Wechsler, N.A. Peppas, R. Langer, Engineering precision nanoparticles for drug delivery, Nat. Rev. Drug Discov. 20 (2021) 101–124, https://doi.org/10.1038/s41573-020-0090-8.

[13] Y. Du, X. Liu, Q. Liang, X.J. Liang, J. Tian, Optimization and design of magnetic ferrite nanoparticles with uniform tumor distribution for highly sensitive MRI/MPI performance and improved magnetic hyperthermia therapy, Nano Lett. 19 (2019) 3618–3626, https://doi.org/10.1021/acs.nanolett.9b00630.

[14] Y. Liang, J. Xie, J. Yu, Z. Zheng, F. Liu, A. Yang, Recent advances of high performance magnetic iron oxide nanoparticles: controlled synthesis, properties tuning and cancer theranostics, Nano Sel. 2 (2021) 216–250, https://doi.org/10.1002/nano.202000169.

[15] M. Salvador, A. Moyano, J.C. Martínez-García, M.C. Blanco-López, M. Rivas, Synthesis of superparamagnetic iron oxide nanoparticles: SWOT analysis towards their conjugation to biomolecules for molecular recognition applications, J. Nanosci. Nanotechnol. 19 (2019) 4839–4856, https://doi.org/10.1166/jnn.2019.16931.

[16] S.A.M.K. Ansari, E. Ficiarà, F.A. Ruffinatti, I. Stura, M. Argenziano, O. Abollino, R. Cavalli, C. Guiot, F. D'Agata, Magnetic iron oxide nanoparticles: synthesis, characterization and functionalization for biomedical applications in the Central Nervous System, Materials 12 (2019), https://doi.org/10.3390/ma12030465.

[17] L. Qiao, Z. Fu, J. Li, J. Ghosen, M. Zeng, J. Stebbins, P.N. Prasad, M.T. Swihart, Standardizing size- and shape-controlled synthesis of monodisperse magnetite (Fe3O4) nanocrystals by identifying and exploiting effects of organic impurities, ACS Nano 11 (2017) 6370–6381, https://doi.org/10.1021/acsnano.7b02752.

[18] M. Marciello, V. Connord, S. Veintemillas-Verdaguer, M.A. Vergés, J. Carrey, M. Respaud, C.J. Serna, M.P. Morales, Large scale production of biocompatible magnetite nanocrystals with high saturation magnetization values through green aqueous synthesis, J. Mater. Chem. B 1 (2013) 5995, https://doi.org/10.1039/c3tb20949k.

[19] R.R. Massart, Preparation of aqueous magnetic liquids in alkaline and acidic media, IEEE Trans. Magn. 17 (1981) 1247–1248, https://doi.org/10.1109/TMAG.1981.1061188.

[20] L. Li, K.Y. Mak, C.W. Leung, K.Y. Chan, W.K. Chan, W. Zhong, P.W.T. Pong, Effect of synthesis conditions on the properties of citric-acid coated iron oxide nanoparticles, Microelectron. Eng. 110 (2013) 329–334, https://doi.org/10.1016/j.mee.2013.02.045.

[21] A. Bee, R. Massart, S. Neveu, Synthesis of very fine maghemite particles, J. Magn. Magn. Mater. 149 (1995) 6–9, https://doi.org/10.1016/0304-8853(95)00317-7.

[22] M. Abdolrahimi, M. Vasilakaki, S. Slimani, N. Ntallis, G. Varvaro, S. Laureti, C. Meneghini, K.N. Trohidou, D. Fiorani, D. Peddis, Magnetism of nanoparticles: effect of the organic coating, Nanomaterials 11 (2021) 1787, https://doi.org/10.3390/nano11071787.

[23] X. Batlle, C. Moya, M. Escoda-Torroella, Ò. Iglesias, A. Fraile Rodríguez, A. Labarta, Magnetic nanoparticles: from the nanostructure to the physical properties, J. Magn. Magn. Mater. 543 (2022), 168594, https://doi.org/10.1016/j.jmmm.2021.168594.

[24] J.C. Chacón-Torres, C. Reinoso, D.G. Navas-León, S. Briceño, G. González, Optimized and scalable synthesis of magnetic nanoparticles for RNA extraction in response to developing countries' needs in the detection and control of SARS-CoV-2, Sci. Rep. 10 (2020) 1–10, https://doi.org/10.1038/s41598-020-75798-9.

[25] S.B. Somvanshi, P.B. Kharat, T.S. Saraf, S.B. Somwanshi, S.B. Shejul, K.M. Jadhav, Multifunctional nano-magnetic particles assisted viral RNA-extraction protocol for potential detection of COVID-19, Mater. Res. Innov. 25 (2021) 169–174, https://doi.org/10.1080/14328917.2020.1769350.

[26] H. Nosrati, M. Salehiabar, E. Attari, S. Davaran, H. Danafar, H.K. Manjili, Green and one-pot surface coating of iron oxide magnetic nanoparticles with natural amino acids and biocompatibility investigation, Appl. Organomet. Chem. 32 (2018) 1–10, https://doi.org/10.1002/aoc.4069.

[27] S.P. Schwaminger, P.F. García, G.K. Merck, F.A. Bodensteiner, S. Heissler, S. Günther, S. Berensmeier, Nature of interactions of amino acids with bare magnetite nanoparticles, J. Phys. Chem. C 119 (2015) 23032–23041, https://doi.org/10.1021/acs.jpcc.5b07195.

[28] K.C. Barick, P.A. Hassan, Glycine passivated Fe 3O 4 nanoparticles for thermal therapy, J. Colloid Interface Sci. 369 (2012) 96–102, https://doi.org/10.1016/j.jcis.2011.12.008.

[29] A. Antosova, Z. Bednarikova, M. Koneracka, I. Antal, J. Marek, M. Kubovcikova, V. Zavisova, A. Jurikova, Z. Gazova, Amino acid functionalized superparamagnetic nanoparticles inhibit lysozyme amyloid fibrillization, Chem. A Eur. J. 25 (2019) 7501–7514, https://doi.org/10.1002/chem.201806262.

[30] I. Antal, O. Strbak, I. Khmara, M. Koneracka, M. Kubovcikova, V. Zavisova, M. Kmetova, E. Baranovicova, D. Dobrota, MRI relaxivity changes of the magnetic nanoparticles induced by different amino acid coatings, Nanomaterials 10 (2020), https://doi.org/10.3390/nano10020394.

[31] K.C. Barick, S. Singh, D. Bahadur, M.A. Lawande, D.P. Patkar, P.A. Hassan, Carboxyl decorated Fe3O4 nanoparticles for MRI diagnosis and localized hyperthermia, J. Colloid Interface Sci. 418 (2014) 120–125, https://doi.org/10.1016/j.jcis.2013.11.076.

[32] N.C. Feitoza, T.D. Gonçalves, J.J. Mesquita, J.S. Menegucci, M.K.M.S. Santos, J. A. Chaker, R.B. Cunha, A.M.M. Medeiros, J.C. Rubim, M.H. Sousa, Fabrication of glycine-functionalized maghemite nanoparticles for magnetic removal of copper from wastewater, J. Hazard. Mater. 264 (2014) 153–160, https://doi.org/10.1016/j.jhazmat.2013.11.022.

[33] R. Verma, A. Asthana, A.K. Singh, S. Prasad, M.A.B.H. Susan, Novel glycine-functionalized magnetic nanoparticles entrapped calcium alginate beads for effective removal of lead, Microchem. J. 130 (2017) 168–178, https://doi.org/10.1016/j.microc.2016.08.006.

[34] J. You, L. Wang, Y. Zhao, W. Bao, A review of amino-functionalized magnetic nanoparticles for water treatment: features and prospects, J. Clean. Prod. 281 (2021), https://doi.org/10.1016/j.jclepro.2020.124668.

[35] T. Köhler, A. Feoktystov, O. Petracic, E. Kentzinger, T. Bhatnagar-Schöffmann, M. Feygenson, N. Nandakumaran, J. Landers, H. Wende, A. Cervellino, U. Rücker, A. Kovács, R.E. Dunin-Borkowski, T. Brückel, Mechanism of magnetization reduction in iron oxide nanoparticles, Nanoscale 13 (2021) 6965–6976, https://doi.org/10.1039/d0nr08615k.

[36] C. Vázquez-Vázquez, M.A. López-Quintela, M.C. Buján-Núñez, J. Rivas, M.A. Lo, C. Va, J. Rivas, M.C. Buja, Finite size and surface effects on the magnetic properties of cobalt ferrite nanoparticles, J. Nanopart. Res. 13 (2011) 1663–1676, https://doi.org/10.1007/s11051-010-9920-7.

[37] C. Pereira, A.M. Pereira, C. Fernandes, M. Rocha, R. Mendes, M.P. Fernández-García, A. Guedes, P.B. Tavares, J.M. Grenéche, J.P. Araújo, C. Freire, Superparamagnetic MFe 2O 4 (M = Fe, Co, Mn) nanoparticles: tuning the particle size and magnetic properties through a novel one-step coprecipitation route, Chem. Mater. (2012), https://doi.org/10.1021/cm300301c.

[38] E.V. Shelekhov, T.A. Sviridova, Programs for X-ray analysis of polycrystals, Met. Sci. Heat Treat. 42 (2000) 309–313, https://doi.org/10.1007/BF02471306.

[39] G. Muscas, N. Yaacoub, G. Concas, F. Sayed, R. Sayed Hassan, J.M. Greneche, C. Cannas, A. Musinu, V. Foglietti, S. Casciardi, C. Sangregorio, D. Peddis, Evolution of the magnetic structure with chemical composition in spinel iron oxide nanoparticles, Nanoscale 7 (2015) 13576–13585, https://doi.org/10.1039/C5NR02723C.

[40] M.E. Matsnev, V.S. Rusakov, SpectrRelax: an application for Mössbauer spectra modeling and fitting, AIP Conf. Proc. 1489 (2012) 178–185, https://doi.org/10.1063/1.4759488.

[41] M. Coduri, P. Masala, L. Del Bianco, F. Spizzo, D. Ceresoli, C. Castellano, S. Cappelli, C. Oliva, S. Checchia, M. Allieta, D.V. Szabo, S. Schlabach, M. Hagelstein, C. Ferrero, M. Scavini, Local structure and magnetism of Fe2O3 maghemite nanocrystals: the role of crystal dimension, Nanomaterials 10 (2020), https://doi.org/10.3390/nano10050867.

[42] A. Omelyanchik, F.G. da Silva, G. Gomide, I. Kozenkov, J. Depeyrot, R. Aquino, A. F.C. Campos, D. Fiorani, D. Peddis, V. Rodionova, S. Jovanović, Effect of citric acid on the morpho-structural and magnetic properties of ultrasmall iron oxide nanoparticles, J. Alloy. Compd. 883 (2021), 160779, https://doi.org/10.1016/j.jallcom.2021.160779.

[43] M. Stoia, R. Istratie, C. Păcurariu, Investigation of magnetite nanoparticles stability in air by thermal analysis and FTIR spectroscopy, J. Therm. Anal. Calorim. 125 (2016) 1185–1198, https://doi.org/10.1007/s10973-016-5393-y.

[44] X. Ye, D. Lin, Z. Jiao, L. Zhang, The thermal stability of nanocrystalline maghemite, J. Phys. D Appl. Phys. 31 (1998) 2739–2744, https://doi.org/10.1088/0022-3727/31/20/006.

[45] R. Frison, G. Cernuto, A. Cervellino, O. Zaharko, G.M. Colonna, A. Guagliardi, N. Masciocchi, Magnetite–maghemite nanoparticles in the 5–15 nm range: correlating the core–shell composition and the surface structure to the magnetic properties. A total scattering study, Chem. Mater. 25 (2013) 4820–4827, https://doi.org/10.1021/cm403360f.

[46] X. Batlle, N. Pérez, P. Guardia, O. Iglesias, A. Labarta, F. Bartolomé, L.M. Garca, J. Bartolomé, A.G. Roca, M.P. Morales, C.J. Serna, Magnetic nanoparticles with bulklike properties (invited), J. Appl. Phys. 109 (2011) 1–7, https://doi.org/10.1063/1.3559504.

[47] W. Baaziz, B.P. Pichon, S. Fleutot, Y. Liu, C. Lefevre, J.M. Greneche, M. Toumi, T. Mhiri, S. Begin-Colin, Magnetic iron oxide nanoparticles: reproducible tuning of the size and nanosized-dependent composition, defects, and spin canting, J. Phys. Chem. C 118 (2014) 3795–3810, https://doi.org/10.1021/jp411481p.

[48] K. Sartori, D. Gailly, C. Bouillet, J.M. Grenèche, P. Dueñas-Ramirez, S. Begin-Colin, F. Choueikani, B.P. Pichon, Increasing the size of Fe3-δO4 nanoparticles by performing a multistep seed-mediated growth approach, Cryst. Growth Des. 20 (2020) 1572–1582, https://doi.org/10.1021/acs.cgd.9b01300.

[49] H. Sharifi Dehsari, V. Ksenofontov, A. Möller, G. Jakob, K. Asadi, Determining magnetite/maghemite composition and core-shell nanostructure from magnetization curve for iron oxide nanoparticles, J. Phys. Chem. C 122 (2018) 28292–28301, https://doi.org/10.1021/acs.jpcc.8b06927.

[50] I.J. Bruvera, P. Mendoza Zélis, M. Pilar Calatayud, G.F. Goya, F.H. Sánchez, Determination of the blocking temperature of magnetic nanoparticles: the good, the bad, and the ugly, J. Appl. Phys. 118 (2015), 184304, https://doi.org/10.1063/1.4935484.

[51] J.S. Micha, B. Dieny, J.R. Régnard, J.F. Jacquot, J. Sort, Estimation of the Co nanoparticles size by magnetic measurements in Co/SiO2 discontinuous multilayers, J. Magn. Magn. Mater. 272–276 (2004) 2003–2004, doi:10.1016/j.jmmm.2003.12.268.

[52] S. Mørup, M.F. Hansen, C. Frandsen, 1.04 magnetic nanoparticles, in: Comprehensive Nanoscience and Nanotechnology, Elsevier, 2019, pp. 89–140, https://doi.org/10.1016/B978-0-12-803581-8.11338-4.

[53] A.S. Kamzin, I.M. Obaidat, A.A. Valliulin, V.G. Semenov, I.A. Al-Omari, The composition and magnetic structure of Fe3O4/γ-Fe2O3 core–shell nanocomposites at 300 and 80 K: Mössbauer study (Part I), Phys. Solid State 62 (2020) 1933–1943, https://doi.org/10.1134/S1063783420100157.

[54] A.S. Kamzin, I.M. Obaidat, A.A. Valliulin, V.G. Semenov, I.A. Al-Omari, The composition and magnetic structure of Fe3O4/γ-Fe2O3 Core-Shell nanocomposites under external magnetic field: Mössbauer study (Part II), Phys. Solid State 62 (2020) 2167–2172, https://doi.org/10.1134/S1063783420110153.

[55] D.K. Kim, M. Mikhaylova, Y. Zhang, M. Muhammed, Protective coating of superparamagnetic iron oxide nanoparticles, Chem. Mater. 15 (2003) 1617–1627, https://doi.org/10.1021/cm021349j.

[56] P.B. Rathod, A.K. Pandey, S.S. Meena, A.A. Athawale, Quaternary ammonium bearing hyper-crosslinked polymer encapsulation on Fe 3 O 4 nanoparticles, RSC Adv. 6 (2016) 21317–21325, https://doi.org/10.1039/C6RA01543C.

[57] J.B. Mamani, L.F. Gamarra, G.E. De Souza Brito, Synthesis and characterization of Fe3O4 nanoparticles with perspectives in biomedical applications, Mater. Res. 17 (2014) 542–549, https://doi.org/10.1590/S1516-14392014005000050.

[58] J. García, G. Subías, The Verwey transition—a new perspective, J. Phys. Condens. Matter 16 (2004) R145–R178, https://doi.org/10.1088/0953-8984/16/7/R01.

[59] I.S. Lyubutin, A.O. Baskakov, S.S. Starchikov, K.Y. Shih, C.R. Lin, Y.T. Tseng, S. S. Yang, Z.Y. Han, Y.L. Ogarkova, V.I. Nikolaichik, A.S. Avilov, Synthesis and characterization of graphene modified by iron oxide nanoparticles, Mater. Chem. Phys. 219 (2018) 411–420, https://doi.org/10.1016/j.matchemphys.2018.08.042.

[60] M. Rubinstein, D.W. Forester, Investigation of the insulating phase of magnetite by NMR and the Mössbauer effect, Solid State Commun. 9 (1971) 1675–1679, https://doi.org/10.1016/0038-1098(71)90339-5.

[61] R.S. Hargrove, W. Kündig, Mössbauer measurements of magnetite below the Verwey transition, Solid State Commun. 8 (1970) 303–308, https://doi.org/10.1016/0038-1098(70)90455-2.

[62] M. Mizoguchi, Charge and orbital ordering structure of Fe3O4 in the low-temperature phase as deduced from NMR study, J. Phys. Soc. Jpn. 70 (2001) 2333–2344, https://doi.org/10.1143/JPSJ.70.2333.

[63] I. Dézsi, C. Fetzer, Á. Gombkötő, I. Szűcs, J. Gubicza, T. Ungár, Phase transition in nanomagnetite, J. Appl. Phys. 103 (2008) 104312, https://doi.org/10.1063/1.2937252.

[64] R. Řezníček, V. Chlan, H. Štěpánková, P. Novák, Hyperfine field and electronic structure of magnetite below the Verwey transition, Phys. Rev. B Condens. Matter Mater. Phys. 91 (2015) 1–10, https://doi.org/10.1103/PhysRevB.91.125134.

[65] M.S. Senn, J.P. Wright, J.P. Attfield, Charge order and three-site distortions in the Verwey structure of magnetite, Nature 481 (2012) 173–176, https://doi.org/10.1038/nature10704.

[66] B.J. Evans, S.S. Hafner, 57 Fe hyperfine fields in magnetite (Fe 3 O 4), J. Appl. Phys. 40 (1969) 1411–1413, https://doi.org/10.1063/1.1657696.

[67] A.S. Kamzin, I.M. Obaidat, A.A. Valliulin, V.G. Semenov, I.A. Al-Omari, C. Nayek, Mössbauer studies of the structure of core/shell Fe3O4/γ-Fe2O3 nanoparticles, Tech. Phys. Lett. 45 (2019) 426–429, https://doi.org/10.1134/S1063785019050079.

[68] F. Van Der Woude, G.A. Sawatzky, Hyperfine magnetic fields at Fe57 nuclei in ferrimagnetic spinels, Phys. Rev. B 4 (1971) 3159–3165, https://doi.org/10.1103/PhysRevB.4.3159.

[69] S. Mørup, Spin-canting and transverse relaxation at surfaces and in the interior of ferrimagnetic particles, J. Magn. Magn. Mater. 266 (2003) 110–118, https://doi.org/10.1016/S0304-8853(03)00462-1.

[70] E. Lima, A.L. Brandl, A.D. Arelaro, G.F. Goya, Spin disorder and magnetic anisotropy in Fe3O4 nanoparticles, J. Appl. Phys. 99 (2006), 083908, https://doi.org/10.1063/1.2191471.

[71] Y. Yafet, C. Kittel, Antiferromagnetic arrangements in ferrites, Phys. Rev. 87 (1952) 290–294, https://doi.org/10.1103/PhysRev.87.290.

[72] E. Tronc, A. Ezzir, R. Cherkaoui, C. Chanéac, M. Noguès, H. Kachkachi, D. Fiorani, A.M. Testa, J.M. Grenèche, J.P. Jolivet, Surface-related properties of γ-Fe2O3 nanoparticles, J. Magn. Magn. Mater. 221 (2000) 63–79, https://doi.org/10.1016/S0304-8853(00)00369-3.

[73] G.F. Goya, E.R. Leite, Ferrimagnetism and spin canting of Zn 57Fe2O4 nanoparticles embedded in ZnO matrix, J. Phys. Condens. Matter 15 (2003) 641–651, https://doi.org/10.1088/0953-8984/15/4/305.

[74] S. Linderoth, P.V. Hendriksen, F. Bødker, S. Wells, K. Davies, S.W. Charles, S. Mørup, On spin-canting in maghemite particles, J. Appl. Phys. 75 (1994) 6583–6585, https://doi.org/10.1063/1.356902.

[75] E.S. Vasil'eva, O.V. Tolochko, V.G. Semenov, V.S. Volodin, D. Kim, Mössbauer spectroscopy analysis of the phase composition of iron-based nanoparticles, Tech. Phys. Lett. 33 (2007) 40–43, https://doi.org/10.1134/S1063785007010117.

[76] A.F. Lehlooh, S.H. Mahmood, Mössbauer spectroscopy of Fe3O4 ultrafine particles, J. Magn. Magn. Mater. 151 (1995) 163–166, https://doi.org/10.1016/0304-8853(95)00385-1.

[77] U. Klekotka, E. Wińska, D. Satuła, B. Kalska-Szostkoa, Mössbauer studies of surface modified magnetite particles, Acta Phys. Pol. A 134 (2018) 1003–1006, https://doi.org/10.12693/APhysPolA.134.1003.

[78] Z. Surowiec, M. Budzyński, K. Durak, G. Czernel, Synthesis and characterization of iron oxide magnetic nanoparticles, Nukleonika 62 (2017) 73–77, https://doi.org/10.1515/nuka-2017-0009.

[79] P. Burnham, N. Dollahon, C.H. Li, A.J. Viescas, G.C. Papaefthymiou, Magnetization and specific absorption rate studies of ball-milled iron oxide nanoparticles for biomedicine, J. Nanopart. 2013 (2013) 1–13, https://doi.org/10.1155/2013/181820.

[80] R.R. Gabbasov, V.M. Cherepanov, M.A. Chuev, M.A. Polikarpov, V.Y. Panchenko, Size effect of Mössbauer parameters in iron oxide nanoparticles, Hyperfine Inter. 226 (2014) 383–387, https://doi.org/10.1007/s10751-013-0960-0.